Flow Around a Simplified Car, Part 1: Large Eddy Simulation

Siniša Krajnović
e-mail: sinisa@chalmers.se

Lars Davidson

Division of Fluid Dynamics,
Department of Applied Mechanics,
Chalmers University of Technology,
SE-412 96 Gothenburg, Sweden

Large eddy simulations (LES) were made of flows around a generic ground vehicle with sharp edges at the rear end (an Ahmed body with a 25° angle of the rear slanted surface). Separation of the flow at the rear results in large regions with recirculating flow. As the separation is determined by the geometry, the Reynolds number effects are minimized. Resolution requirements of this recirculating flow are smaller than those in LES of wall attached flows. These two consequences of the geometry of the body are used to predict the experimental flow at relatively high Reynolds number. Recommendations are presented for the preparation and realization of LES for vehicle flows. Comparison of the LES results with the experimental data shows good agreement.
[DOI: 10.1115/1.1989371]

Keywords: Large Eddy Simulation, LES, Generic Car Body, Vehicle Aerodynamics, Ground Vehicle

1 Introduction

It has long been known that the shape of ground vehicles determines their aerodynamic properties. A modification of the shape that produces better aerodynamic properties requires a thorough understanding of turbulent flows around vehicles. Unfortunately, after several decades of experimental and numerical studies, our understanding of the flow around ground vehicles is still often limited to a qualitative picture of the time-averaged large flow structures. Experimental techniques were first adopted in studies of flows around ground vehicles and are still more commonly used than numerical methods in the design. Although numerical simulations have been conducted in automobile companies, they were unable until some 10 years ago to predict the flow with the same level of accuracy as wind tunnel tests. Only recently have numerical simulations taken over the role of some experimental studies and become a design tool in some of the automobile companies (such as Volvo Cars). Experimental and numerical methods both have their advantages and disadvantages. Measuring techniques are limited to a part of the domain and are often used to measure time-averaged flow rather than the temporal development of the instantaneous flow. It should be mentioned, however, that it is now possible to study instantaneous flows in a single plane using the particle image velocimetry (PIV) technique. Computational fluid dynamics (CFD) can easily provide spatial information about the flow in the entire domain (virtual wind tunnel). Before we discuss the ability of CFD to predict the development of the flow in time (i.e., temporal information), it is appropriate to make some remarks about the CFD results.

Turbulent scales in the flow around a ground vehicle range from those of the size of the vehicle to microscopic ones. Unfortunately most turbulent scales in this flow are small owing to high Reynolds number, making resolution requirements very high. This makes the solution of time-dependent Navier-Stokes equations for the flows around ground vehicles at operating velocities infeasible. As a result of the limitations in computer resources, simulations of time-averaged Reynolds Averaged Navier-Stokes (RANS) equations have chiefly been used in the literature.

Instead of using real vehicles, very simplified (generic) vehicle models are used in research to study how flow changes with geometry. Using such an approach we can isolate a few geometric properties and study their influence on the flow.

Contributed by the Fluids Engineering Division for publication in the JOURNAL OF FLUIDS ENGINEERING. Manuscript received by the Fluids Engineering Division, July 26, 2004; final revision: May 12, 2005. Associate Editor: Ismail B. Celik.

The objective of the pioneer work of Ahmed et al. [1] was to study the influence of the angle between the roof and the rear end slanted surface of a car with a typical fastback geometry (such as the Volkswagen Golf I or Volkswagen Polo I) on the flow. Their investigation showed a clear influence of the rear slant angle to the time-averaged flow structures. As they varied this angle they found that the flow changes character at an angle of about 30°, which prompted researchers to make further experimental and numerical studies of this flow. Some of the experimental studies are described in [2,3]. Numerical studies such as those in [4,5] are used to validate the CFD technique (often a RANS simulation). A large number of RANS simulations (using different turbulence models) and one large eddy simulation (LES) of the flow around the body defined by Ahmed et al. [1] are presented in [5]. Only two angles of the rear slanted surface, 25° and 35°, were considered in these simulations. The results of the simulations were compared with the experimental data produced by Lienhart and Becker [3]. The main conclusion drawn from these simulations was that, while the simulations were relatively successful in their prediction of the 35° case, they were unsuccessful in the 25° case.

The aim of this paper is to demonstrate that, if carefully applied, the LES can give an accurate representation of the flow around this generic car body characterized by the sharp edges at the rear and the rear slant angle of 25°.

2 Generic Ground Vehicle Body

The generic vehicle body was chosen to be the same as in the experiments of Ahmed et al. [1] and Lienhart and Becker [3]. The geometry of the body and the computational domain are given in Fig. 1. All the geometric quantities are normalized with the body height, H, equal to 0.288 m. The values of the geometric quantities are $l_r/H=2.928$, $G/H=0.697$, and $W/H=1.35$. The front part is rounded with a radius of $R/H=0.347$ in the planes, $y=0$ and $z=0$. The geometry of the rounded corners was made from the data (in the form of distinct points) measured at the body used in Ahmed et al. [1] and Lienhart and Becker [3]. This body is placed in the channel with a cross section of $B\times F=6.493H\times 4.861H$ (width $\times$ height). The cross section of this channel is identical to the open test section of the wind tunnel used in the experiments of Lienhart and Becker [3]. The front face of the body is located at a distance of $x_1=7.3H$ from the channel inlet and the downstream length between the rear face of the body, and the channel outlet is $x_2=21H$. The body is lifted from the floor, producing a ground clearance of $c/H=0.174$, as in the experiments. The Reynolds number, based on the incoming velocity, U_∞, and the car height,

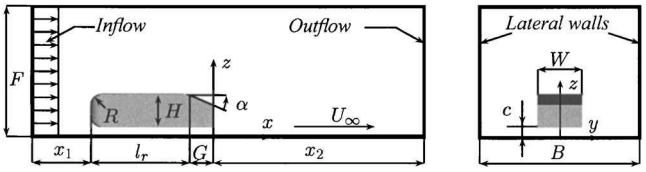

Fig. 1 Schematic representation of the computational domain with vehicle body. Left: view from the side; right: view from behind the body.

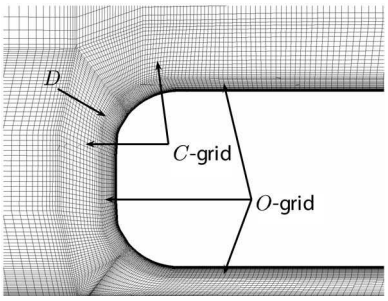

Fig. 2 The computational grid in symmetry plane $y=0$. *D* indicates the position of the dummy surface. View from the side of the front part of the body.

H, of $\mathrm{Re}=7.68\times10^5$ used in the experiments [3] was reduced to $\mathrm{Re}=2\times10^5$. Krajnović and Davidson [6] have already demonstrated successful LES of this lower Reynolds number case with no rear body slant angle, i.e., $\alpha=0°$ (generic bus body). We expect that the slanted rear end will produce a wide spectrum of turbulent scales that must be resolved in LES.

3 Making Large Eddy Simulation

Resolution requirements of the near-wall regions in attached flows such as channel flow or a flat plate flow are similar to those in direct numerical simulations. This is because the coherent structures (so called low- and high-speed streaks) near the walls are responsible for most of the turbulence production in the boundary layer. Thus an accurate representation of these structures is crucial to the results of the LES of the flat plate flow, for example.

Flows around bluff bodies such as those around ground vehicles are different from channel or flat plate flows. They contain a number of separating regions with large coherent structures that contain much more turbulent energy than the near-wall structures. Let us consider the following question. What is the size of the smallest turbulent structures that must be resolved in a LES of the flow around ground vehicles?

In the regions of separated flow (such as the wake behind the vehicle) the transport of momentum is dominated by large recirculating motions of the flow and there is limited influence of the small near-wall structures. Thus the structures that must be resolved in this region are the smallest "large" (recirculating) structures. What is the case for the attached regions in the flow around the vehicle? Prediction of drag is often the main objective of CFD studies in vehicle aerodynamics. As the pressure drag is much larger than the friction drag and is dominated by the low pressure in the wake, prediction of the wake flow is crucial. Does this mean that it is sufficient to predict the wake flow and ignore the resolution requirements for the regions located upstream from the wake? The wake flow is influenced by the upstream flow (and vice versa), but the question is how strong this influence is. The boundary layer developed on the roof surface of the body separates at the location where the roof goes over to the rear face of the body. We can distinguish between two main situations. First, the changeover from the roof to the rear face can be continuous, such as that in a circular cylinder. In that case the position of the separation and the nature of the downstream flow are determined by the upstream history of the flow. The second situation is that in which the geometry defines the separation of the flow, such as in the generic car body studied in this paper. How great is the influence of the upstream flow on the wake in this case? Is the resolution of the upstream boundary layer equally important here as in the case of the continuous changeover in the surface geometry? We believe that in this case the influence of the geometry (i.e., separation defined by the sharp edges) is much greater than that of the upstream history of the flow.

3.1 Our Approach. Although we assume that the upstream boundary layer has limited influence on the flow in the wake, in the flow around our generic car body, we cannot neglect it. Thus we should try to predict the flow in the near-wall region as well as possible. The near-wall coherent structures unfortunately decrease in size with the Reynolds number and the task of resolving these structures is overwhelming for the Reynolds number of 7.68×10^5 used in the experiments by Lienhart and Becker [3] (see [7] for the estimate of the computational cost for the resolution of the near-wall structures in the flow around a ground vehicle body).

We have already assumed that the geometry rather than the upstream flow defines the flow in the wake, which means that we can reduce the Reynolds number in our LES and obtain a flow similar to that in the experiment characterized by the higher Reynolds number. We emphasize that this is only an assumption.

If our hypothesis of Reynolds number independence of the wake flow is correct, how much can we reduce the Reynolds number and still obtain this independence? This is not clear, but the simulated flow on the roof should be as similar as possible to that in the experiment at high Reynolds number. Thus if the high Reynolds number roof flow does not separate at the leading edge, our simulated low Reynolds number flow should not separate or should have as small separated regions as possible. Our knowledge of the dependence of the Reynolds number and the shape of the front of the ground vehicle (i.e., roundedness of the leading edges) is poor and is limited to the dependence of the drag coefficient on the Reynolds number and the roundedness of the leading edges of prismatic bodies [8]. The issue of leading flow separation is discussed in the present paper when the results are reported.

The spatial resolution in the y direction on the top and the roof, and in the z direction on the lateral sides required for LES, could not be obtained for the Reynolds number of 7.68×10^5 used in the experiments [3]. We assume that this Reynolds number can be decreased because of the sharp edges on the rear of the body. Krajnović and Davidson [6] showed that LES can predict the flow around the ground vehicle body that is characterized by a Reynolds number of about 2×10^5 (based on the height of the body and the velocity at the inlet). Thus we choose for our LES the Reynolds number of 2×10^5 instead of the experimental 7.68×10^5.

3.2 Preparation and Realization of LES. Most LES of the flow around bluff bodies use structured hexahedral grids, which give better accuracy than, for example, tetrahedral grids. Making a structured hexahedral grid such that the computational cells are concentrated where they are needed is far from trivial, even around a relatively simple bluff body such as the ground vehicle body studied in this paper. Providing the optimal structured grid for the detailed passenger car is quite a challenge.

Here we shall demonstrate one of the approaches that can be used to concentrate most of the cells in the region around the body. Instead of using only H grid topology, which spreads the fine resolution in the boundary layer of the body all the way to the boundaries of the wind tunnel, we use a combination of O and C grid topologies (see Fig. 2) which enables local refinement of the grid. The topology of the grid consists of an O grid with a thick-

ness of $0.1H$ and a C grid around the O grid (see Fig. 2). An additional "dummy" car surface was made around the surface of the car, and the O grid was projected on these two surfaces. The rest of the blocking structure was made using H grids. This strategy resulted in the following distribution of the computational cells. The O grid (i.e., the region in a belt of thickness $0.1H$ around the body) contained 4.4 and 7.5 million cells with a total of 9.6 and 16.5 million cells in the medium and the fine grids, respectively. The regions containing the O and the C grids together (i.e., the region in a belt of a thickness of $0.28H$ around a car) hold 6.3 and 10.8 million cells in the medium and the fine grids, respectively.

Unlike the results of steady RANS simulations, the results of time-dependent LES are dependent on the time at which we start to monitor our results (i.e., when the fully developed flow is obtained). Unfortunately, in LES of the flow around ground vehicles, the fully developed flow is unknown and must be estimated. The initial fully developed flow is often computed from the fluid at rest (as in this paper) or from a previous solution of a RANS simulation. How do we know that the flow has become fully developed? The only way to be sure that the flow has developed is probably the a posteriori one (i.e., after the entire simulation). Such a test could prove that the mean, rms values, and the spectral picture of the solution are not dependent on the position in time at which we started the sampling of the solution. As we need to start the time averaging before we can perform the a posteriori test, some approximate method must be used to ensure that the characteristics of the flow are not changing. We monitored the time required for the fluid particle to travel from the front to the rear face of the car body. We then computed the mean and the rms values of the global quantities (aerodynamic forces) and local variables (velocity components and pressure in several points in and around the wake behind the body) for this time interval. The time averaging was started when no significant differences were found between two consequent time sequences. The computational cost of obtaining the fully developed flow is significant and, for the simulations presented in this paper, the computational times for obtaining fully developed conditions were roughly one-fourth of the total time of the simulations.

When the flow has evolved to become fully developed, monitoring of the instantaneous results and their averaging can begin. Numerical time steps in LES are short to retain accuracy. The short time steps lead to large number of time steps for resolving the low-frequency events and the time averaging. Our experience is that the number of time steps required for resolving the low-frequency events is larger than that needed for obtaining the time-averaged results [6]. The symmetry of the flow around the symmetry plane ($y=0$ plane) was used in this paper as proof of a sufficiently long averaging time.

4 Governing Equations and Subgrid-Scale Modeling

The governing LES equations are the incompressible Navier-Stokes and the continuity equations filtered with the implicit spatial filter of characteristic width Δ (Δ is the grid resolution in this work):

$$\frac{\partial \bar{u}_i}{\partial t} + \frac{\partial}{\partial x_j}(\bar{u}_i \bar{u}_j) = -\frac{1}{\rho}\frac{\partial \bar{p}}{\partial x_i} + \nu \frac{\partial^2 \bar{u}_i}{\partial x_j \partial x_j} - \frac{\partial \tau_{ij}}{\partial x_j} \tag{1}$$

and

$$\frac{\partial \bar{u}_i}{\partial x_i} = 0. \tag{2}$$

Here, $\bar{u}_i$ and $\bar{p}_i$ are the resolved velocity and pressure, respectively, and the bar over the variable denotes filtering.

These equations are derived applying a filtering operation

$$\bar{f}(x_i) = \int_\Omega f(x_i')G(x_i, x_i')dx_i' \tag{3}$$

on the Navier-Stokes and the continuity equations. Here G is a top hat filter function and Ω represents the entire flow domain. The filtered variables in the governing Eqs. (1) and (2) are obtained implicitly through the spatial discretization.

The goal of the filtering is to decompose the fluid motion into a large-scale component that is resolved and the small subgrid scale (SGS) where the latter is modeled. The influence of the small scales of the turbulence on the large energy carrying scales in Eq. (1) appears in the SGS stress tensor, $\tau_{ij} = \overline{u_i u_j} - \bar{u}_i \bar{u}_j$. The algebraic eddy viscosity model originally proposed by Smagorinsky [9] is used in this paper for its simplicity and low computational cost. The Smagorinsky model represents the anisotropic part of the SGS stress tensor, τ_{ij}, as

$$\tau_{ij} - \tfrac{1}{3}\delta_{ij}\tau_{kk} = -2\nu_{sgs}\bar{S}_{ij} \tag{4}$$

where $\nu_{sgs} = (C_s f \Delta)^2 |\bar{S}|$ is the SGS viscosity,

$$\bar{S}_{ij} = \frac{1}{2}\left(\frac{\partial \bar{u}_i}{\partial x_j} + \frac{\partial \bar{u}_j}{\partial x_i}\right) \tag{5}$$

is the resolved rate-of-strain tensor, and $|\bar{S}| = (2\bar{S}_{ij}\bar{S}_{ij})^{1/2}$. f in the expression for the SGS viscosity is the van Driest damping function

$$f = 1 - \exp\left(\frac{n^+}{25}\right), \tag{6}$$

where n is the wall normal distance. Using this damping function, wall effects are partially taken into account by "damping" length scale $l = C_s\Delta$ near the walls. The value of $C_s = 0.1$ previously used for bluff-body flows [10] and flow around a simplified bus [7,6] is used in this work. The filter width, Δ, is defined in this work as $\Delta = (\Delta_1\Delta_2\Delta_3)^{1/3}$, where Δ_i are the computational cell sizes in three coordinate directions.

5 Boundary Conditions and Numerical Details

The average turbulent intensity at the inlet of the wind tunnel used in the experiments of Lienhart and Becker [3] was low (0.25%). A uniform velocity profile, U_∞, constant in time was thus used as the inlet boundary condition in our LES. The convective boundary condition $\partial \bar{u}_i/\partial t + U_\infty(\partial \bar{u}_i/\partial x) = 0$ was used at the downstream boundary. The lateral surfaces and the ceiling were treated as slip surfaces using symmetry conditions ($\partial \bar{u}/\partial y = \partial \bar{w}/\partial y = \bar{v} = 0$ for the lateral sides and $\partial \bar{u}/\partial z = \partial \bar{v}/\partial z = \bar{w} = 0$ for the ceiling). This boundary condition is different from the experimental one, where the test section had a floor but no lateral sides or ceiling. The consequence of this boundary condition is that the flow across the lateral sides and the ceiling is permitted in the experiment but not in the simulation, resulting in different "effective" blocking of the cross section. This will probably have some influence on the aerodynamic forces. No-slip boundary conditions were used on the surface of the body and the instantaneous wall functions based on the log-law (see [6] for details) were applied on the channel floor.

The experimental setup included a turbulent trip wire that was glued around the entire circumference close to the front end of the model and that makes the flow relatively Reynolds number independent. Unfortunately the exact position of this trip wire is not known, and it is not clear how to model this trip wire in our simulation. The trip wire was neither modeled nor included in the present study.

Numerical accuracy was established by making three LES on different computational grids containing 3.5, 9.6, and 16.5 million nodes. The fine computational grid (containing 16.5 million nodes) has a wall normal resolution of $n^+ < 0.33, 13 < \Delta s^+ < 250$ in the streamwise direction and $23 < \Delta l^+ < 70$ in the direction par-

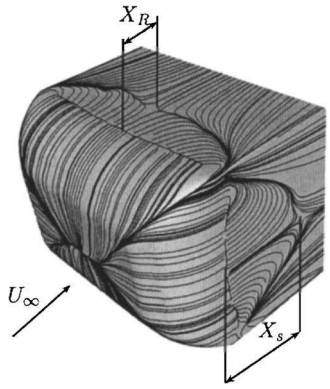

Fig. 3 Time-averaged trace lines on the surface of the front part of the body showing the extensions of the roof vortex, X_R, and the lateral vortex, X_s

allel with the surface of the body and normal to the streamwise direction (the mean Δl^+ is around 30). Here $\Delta n^+ = \Delta n \langle u_\tau \rangle_t / \nu$, $\Delta s^+ = \Delta s \langle u_\tau \rangle_t / \nu$, $\Delta l^+ = \Delta l \langle u_\tau \rangle_t / \nu$ and $\langle u_\tau \rangle_t$ is the time-averaged friction velocity. The time step was 1×10^{-4}, giving a maximum CFL number of approximately 0.9. The averaging time, tU_∞ / H, in the simulations was 38.2 (110,000 time steps).

6 Numerical Method

Equations (1) and (2) are discretized using a 3D finite volume method for solving the incompressible Navier-Stokes equations using a collocated grid arrangement [11]. Both convective and viscous plus subgrid fluxes are approximated by central differences of second-order accuracy. The time integration is done using the second-order Crank-Nicolson scheme. Although no explicit dissipation is added to prevent odd-even decoupling, an implicit dissipation is present. This is done by adding the difference between the pressure gradient at the face and the node. It can be shown that this term is proportional to the third derivative of pressure, i.e., $\partial^3 p / \partial x_i^3$. This term corresponds to Rhie-Chow dissipation [12]. The SIMPLEC algorithm is used for the pressure-velocity coupling. The code is parallelized using block decomposition and the MPI message passing system [13].

7 Results

Our LES resulted in a large amount of instantaneous and time-averaged data. Presenting all these results in a systematic way requires dividing the results among two papers. In this paper we concentrate on presenting the comparison of the LES and the experimental data. The three LES on different grids will be compared among themselves and the influence of the grid refinement will be studied. In the second paper [14] we use our results to describe both the instantaneous and the time-averaged flows in details.

7.1 Global Quantities. This section presents the lengths of the recirculating regions and the aerodynamic forces. Both the time-averaged and the rms values of the forces are reported. Results of our three LES are compared with the experimental data (when available).

As will be demonstrated in the second paper [14], the flow separates at the front end of the body (see Fig. 3). The length of the separation region on the roof, X_R, is equal to $0.23H$, $0.15H$, and $0.08H$ in the LES using coarse, medium, and fine grids, respectively. The separation region, R, on the roof is very thin, with a thickness of $0.0052H$, $0.0024H$, and $0.0024H$ in the LES using coarse, medium, and fine grids, respectively. On the lateral sides we have measured X_s to be equal to $0.52H$, $0.295H$, and $0.128H$, in the coarse, medium, and fine grid LES, respectively. This separation region is thicker than the separation region on the roof. Its

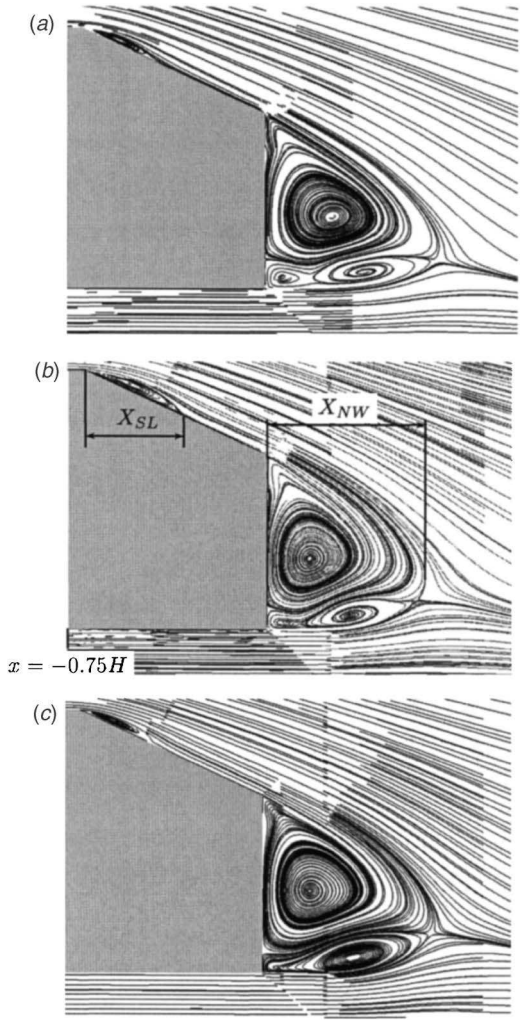

Fig. 4 Time-averaged streamlines projected onto symmetry plane $y=0$ of the car body from LES using (*a*) coarse grid, (*b*) medium grid, and (*c*) fine grid. View is from the lateral side of the body.

thickness is $0.0086H$, $0.0038H$, and $0.0038H$ in the coarse, medium, and fine grid LES, respectively. Finally, we found that the flow separates at the lower rounded edge in the LES using the fine grid. This resulted in the separation region on the underbody that has a maximal extension in the streamwise direction equal to $0.049H$ and a thickness of $0.00035H$ (at $y=-0.347H$). Thus this separation region is about one order of magnitude thinner and shorter than those on the roof and the lateral sides of the body. Both LES using coarse and medium grids produced an attached flow in this region.

The only experimental data on the separation lengths on the front end of the body come from the oil-film visualization of the flow characterized by a Reynolds number of 1.71×10^5 [15]. They measured the length of the recirculating region equal to $0.2175H$ (it is not clear from their paper whether this is the length of the region on the roof or the lateral sides.).

Let us now consider the predicted near-wake flow from our simulations. Figure 4 shows a comparison of the time-averaged streamlines projected onto the symmetry plane, $y=0$, from our LES using different grids. We found that the length from the separation on the upper edge of the rear slant surface to the reattachment, X_{SL}, was approximately equal to $0.28H$, $0.3H$, and $0.35H$ in the coarse, medium, and fine grid LES, respectively. The extension of the near-wake separation bubble (X_{NW} in Fig. 4) obtained

Table 1 Time-averaged pressure drag ($\langle C_D\rangle_t$), and lift ($\langle C_L\rangle_t$) coefficients, and pressure coefficients integrated on the front ($\langle C_K\rangle_t$), rear slanted ($\langle C_S\rangle_t$), and rear vertical surface ($\langle C_B\rangle_t$). The rms values are denoted with the subscript *RMS* (such as $C_{SF_{RMS}}$ in the rms value of the side force coefficient.)

Case	$\langle C_D\rangle_t$	$C_{D_{RMS}}$	$\langle C_K\rangle_t$	$C_{K_{RMS}}$	$\langle C_S\rangle_t$	$C_{S_{RMS}}$	$\langle C_B\rangle_t$	$C_{B_{RMS}}$	$C_{SF_{RMS}}$	$\langle C_L\rangle_t$	$C_{L_{RMS}}$
coarse	0.288	0.004	0.001	0.001	0.582	0.006	0.234	0.004	0.005	0.334	0.011
medium	0.305	0.007	0.001	0.001	0.648	0.002	0.286	0.009	0.005	0.348	0.018
fine	0.292	0.005	0.001	0.001	0.618	0.009	0.265	0.006	0.005	0.344	0.014

in the coarse, medium, and fine grid simulations was $0.6H$, $0.65H$, and $0.65H$, respectively. The center plane projection of the near wake in Fig. 4(*a*) shows three vortices in the coarse grid simulation. The lower vortex close to the rear face loses its form in the medium grid LES and disappears in the fine grid LES [see Figs. 4(*b*) and 4(*c*)]. Thus this false structure is a result of an inadequate resolution in the coarse and medium grid LES.

7.2 Aerodynamic Forces. We have already mentioned that the boundary conditions for the lateral channel walls are different in the experimental investigations and our LES. This disagreement implies differences in the blockage of the experimental and the numerical wind tunnels, resulting in differences in aerodynamic forces. Thus the comparison of the results between experiments and simulations would require some kind of blockage correction for the forces. An additional difficulty in comparing the numerical and the experimental forces is that Ahmed et al. [1] measured pressure drag only at three angles of the rear slant surface, 5°, 12.5°, and 30°. These values were then used to interpolate pressure drag for all angles between 0° and 30°. Lienhart and Becker [3] did not measure the drag but only the distribution of the pressure coefficient on the rear part of the body. Furthermore, the body used in both experiments had stilts that were omitted in our numerical model. These stilts are responsible for some contribution to the drag measured in the experiment.

In the absence of reliable drag corrections, we present results of the three simulations and discuss their agreement with the experimental values, keeping in mind the differences in the geometry and the blocking of the cross section.

The time history of the aerodynamic force coefficients in all three directions, i.e., the drag, the lift, and the side forces coefficients, were computed as $C_D=D/0.5\rho U_\infty^2 A$, $C_L=L/0.5\rho U_\infty^2 A$, and $C_{SF}=SF/0.5\rho U_\infty^2 A$, respectively. Here ρ is density; D, L, and SF are drag, lift and side force due to the pressure, respectively; and A is the frontal area (note that the reference area for all three coefficients is the same projected frontal area in the streamwise direction). These force coefficients were later used to compute the mean and the rms values presented in Table 1. As expected (owing to higher blockage), all three values of the time-averaged drag coefficients from our LES are higher than the value of $\langle C_D\rangle_t = 0.24$ that can be interpolated from the results of Ahmed et al. [1]. The deviation (rms values) from the mean drag coefficient was found to be around 2% of the mean value in all three simulations (see Table 1). The side force coefficient, C_{SF}, was found to vary by approximately 0.005 in all three simulations. The time-averaged lift force coefficient $\langle C_L\rangle_t$ was relatively independent of the grid refinement, having a value between 0.334 and 0.348. Its rms value was between 3% and 5% of the time-averaged lift force coefficients.

Table 1 shows that the aerodynamic forces from three LES from different grids are not consistent with the grid refinement (i.e., they do not only increase or only decrease with the grid refinement). This inconsistency is a result of a very poor resolution in the coarse grid simulation. Too little turbulent kinetic energy is resolved and too much is left to the subgrid-scale model.

Similar to that which Ahmed et al. [1] did, we integrated the streamwise component of the pressure forces for the front, the rear slanted, and the rear vertical surfaces (see Fig. 5 and Table 1). These were then used to break down the total pressure drag into the contributions from the front, the slanted, and the vertical rear surfaces. The three forces are of course dependent on the positions of the reference pressure, which should be the same in the experimental and the numerical studies. Unfortunately, the position of the reference pressure from the experiment of Ahmed et al. [1] is not known, and the differences in its location may influence our comparison. Table 1 gives the time-averaged forces and their rms values. The force on the rear slanted surface, C_S, was found to dominate the total pressure, followed by the force on the vertical rear surface, C_B. Their rms values were between 3% and 10% and 2% and 3% of the time-averaged values for C_S and C_B, respectively. Breaking down the total pressure drag with the help of C_S and C_B gives the relative contributions presented in Table 2. The contributions of the vertical rear surface, $\langle C_B\rangle_t/\langle C_D\rangle_t$, from the three LES are close to the experimental value of 0.07, but there are large differences between $\langle C_K\rangle_t/\langle C_D\rangle_t=0.018$ and $\langle C_S\rangle_t/\langle C_D\rangle_t=0.146$ measured in [1] and our LES results that are given in Table 2. The contribution of the front part coefficient, C_K, to the total pressure drag is very small (see Tables 1 and 2). The low values of C_K are caused by the separated regions on the leading part that reduce the pressure. It is appropriate to mention that the C_K can even become negative (depending on the roundedness of the front and the choice of the reference pressure), such as in [6].

Again there are many uncertainties in this comparison of the experimental data and our LES results for the aerodynamic forces, and these results should be used only as an indication of the magnitude of the contributions of the integrated pressure on the front, the slanted, and the vertical rear surfaces to the total pressure drag.

The time histories of the integrated pressure coefficients were Fourier transformed and the dominating frequencies were identified. Here we present results of the fine grid simulation. Two dominating frequencies were found in the Fourier transform of the drag coefficient signal. These correspond to Strouhal numbers St =0.15 and St=0.26. The same two frequencies were found in the

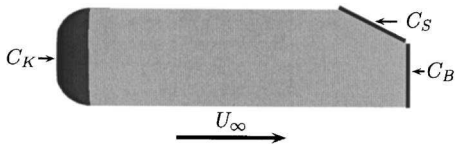

Fig. 5 Schematic representation of the pressure drag breakdown. C_K, C_S, and C_B are integrated pressure force coefficients from the front, the rear slanted, and the rear vertical surfaces, respectively.

Table 2 Relative contributions of the front, rear slanted, and rear vertical surfaces to the total pressure drag (see Fig. 5)

Case	$\langle C_K\rangle_t/\langle C_D\rangle_t$	$\langle C_S\rangle_t/\langle C_D\rangle_t$	$\langle C_B\rangle_t/\langle C_D\rangle_t$
coarse	0.0004	0.205	0.079
medium	0.0004	0.211	0.093
fine	0.0004	0.204	0.088

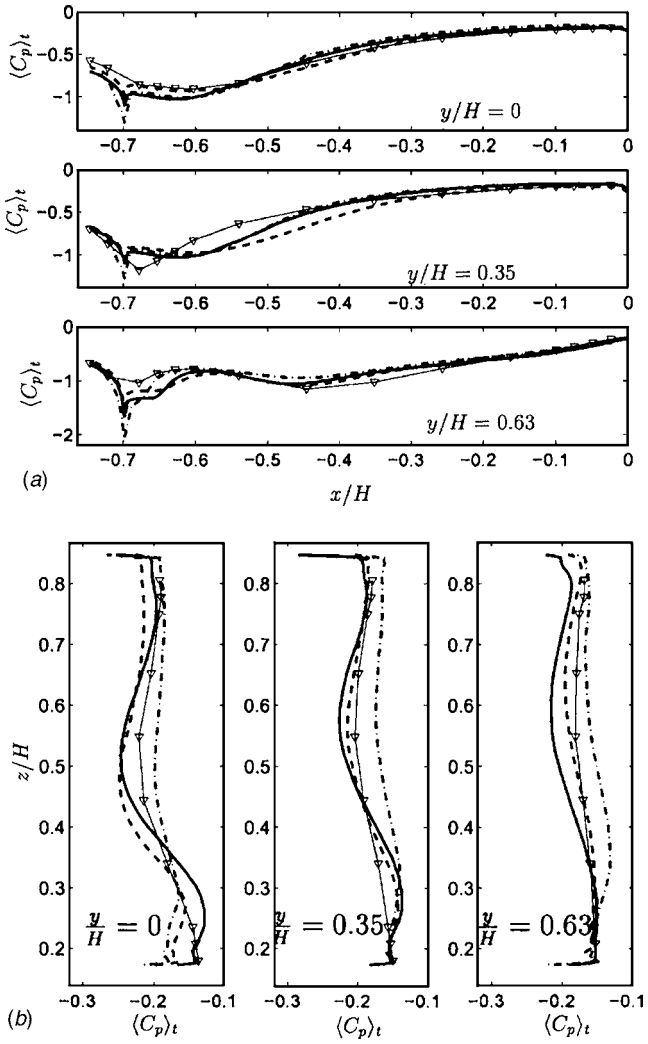

Fig. 6 Distribution of the time-averaged surface pressure coefficients in three planes: $y=0$, $y=0.35H$, and $y=0.63H$. These are plotted along (*a*) the slanted surface and (*b*) the rear vertical surface. Fine grid (solid curve); medium grid (dashed curve); coarse grid (dashed-dotted curve); experiment (symbols).

signal of the pressure coefficient integrated over the rear slanted surface, C_S. This was expected since we found that the pressure drag coefficient is dominated by the surface pressure on the slanted surface (see Table 2). The strongest peak in the Fourier transform of the lift coefficient was found to be at Strouhal number St=0.23 but there were also three other peaks at St=0.1, 0.38, and 0.5 of similar magnitude. The side force signal is very irregular and lacks any dominating frequency in its Fourier transform.

Instead of comparing the results for integrated pressure coefficients C_S and C_B described above, it is probably better to make a comparison of the shapes of the pressure coefficient on the rear slanted and the vertical surfaces. For this comparison we use the data of Lienhart and Becker [3]. As reference pressure they took the static pressure in the undisturbed flow upstream of the model close to the exit of the contraction [16] (the exact position is not reported). The reference pressure in our simulations was taken at the inlet close to the left lateral wall of the channel at $z=2F/3$ (see Fig. 1). However, as can be seen in Fig. 6(*a*), the predicted and experimental C_p at the trailing edge of the slanted surface ($x/H=0$) agree well.

Profiles of the $\langle C_p \rangle_t$ for three planes ($y=0$, $y=0.35H$, and $y=0.63H$) are shown in Fig. 6. The distribution of the surface pressure coefficients along the rear slanted surface is shown in Fig. 6(*a*). The flow must change direction when it separates on the sharp spanwise edge between the roof and the slanted surface forming the shear layer. This change in the flow direction results in the pressure gradient, and a dip in a surface pressure is formed at the position of the sharp edge ($x/H=-0.698$). This rapid decrease in the surface pressure coefficient $\langle C_p \rangle_t$ was observed in all three simulations in Fig. 6(*a*). The mesh of the pressure taps used in the experiment was too coarse to capture this dip [see Fig. 6(*a*)]. All three LES are in good agreement with the experimental $\langle C_p \rangle_t$ between approximately $x/H=-0.55$ and $x/H=0$ (the position of the rear vertical surface) in the center plane ($y/H=0$). For $x/H<-0.55$ we found that the profiles from LES using coarse and fine grids are lower, while the medium grid LES produced a $\langle C_p \rangle_t$ in good agreement with the experiment. This advantage of the medium grid simulation disappears in plane $y=0.35H$, where the profiles from the fine grid simulation are in better agreement with the experiment. Although the magnitude and the shapes of the fine grid LES are the same as in the experiments for $-0.45 \leqslant x/H \leqslant 0$, they are different for $x/H<-0.45$. Agreement between the simulated and experimental profiles in plane $y=0.63H$ is good, with some differences around the dip in the surface pressure coefficient [see Fig. 6(*a*)].

Surface pressure coefficients on the rear vertical surface are presented in Fig. 6(*b*). Although it appears that the coarse grid LES gives a $\langle C_p \rangle_t$ coefficient in good agreement with the experiment in the center plane ($y=0$), the profile is too flat and the $\langle C_p \rangle_t$ values close to the lower edge of the body are too low as compared with the experimental ones. The curvature of the experimental profile is captured much better in the medium and the fine grid LES. The profiles in plane $y/H=0.35$ from the medium and the fine grid simulations have the same amplitude as the experimental, with slightly lower and higher $\langle C_p \rangle_t$ in the medium and lower parts of the profiles, respectively. The coarse grid simulation predicted too high a surface pressure along the entire length of the surface in this plane. Surprisingly, the medium grid LES gave a prediction of the $\langle C_p \rangle_t$ for $y/H=0.63$ that was in best agreement with the measurements. This "better agreement" of the medium grid profile compared with fine grid profile at this position is probably a matter of coincidence. Although the pressure coefficients from the fine grid LES have lower values than the experimental in this plane, the shapes with only one valley between the lower and upper edges are similar. However, the shape of the coarse grid LES profile is different, showing a hill followed by a valley (from the lower to the upper edges of the surface) compared to the experimental profile.

8 Comparison of the Velocities and Reynolds Stresses

Although we have compared all the profiles for the velocities and the Reynolds stresses available in the data files provided from the experimental work [3], space limitations prevent us from reporting all the results in this paper. We thus choose to present the parts of the results that give a fair representation of the comparison of LES and experiments.

Velocity and Reynolds stresses were measured in [3] using a two-component laser-Doppler anemometer (LDA). In this paper we have chosen to present comparisons of the profiles in three planes, $y=0$, $y=0.35H$ and $y=0.63H$. As we compare LES and experimental profiles, we should keep in mind that the experimental data come from several different experimental runs. As we will show later, we have found some discrepancies between our LES profiles and the experimental data for some positions that came from one data set and no discrepancies for other positions that were almost identical to the former ones but whose experimental data came from another set of experiments. These differences will be discussed in the following text.

Comparisons of the velocity profiles and the Reynolds stresses in plane $y=0$ are presented in Figs. 7 and 8. Figure 7(*a*) shows

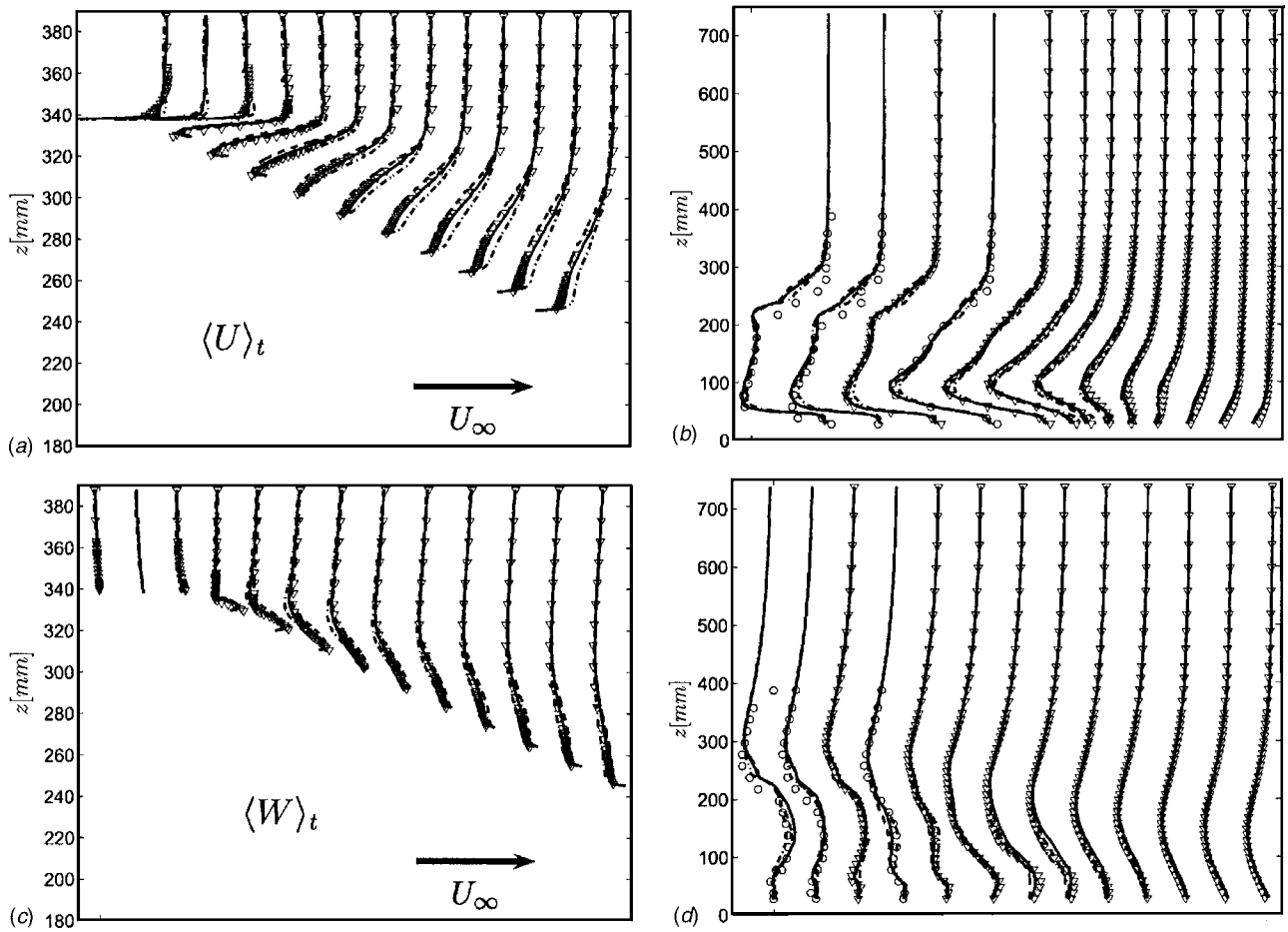

Fig. 7 Time-averaged $\langle U\rangle_t$ [(*a*) and (*b*)] and $\langle W\rangle_t$ [(*c*) and (*d*)] velocity profiles in the symmetry plane ($y=0$). Left: slanted surface; right: wake region. Fine grid (solid curve); medium grid (dashed curve); coarse grid (dashed-dotted curve); experiment (symbols).

streamwise velocity profiles $\langle U\rangle_t$ on the roof and the slanted surface for positions between $x=-0.844H$ and $x=-0.01H$ (from left to right), where the space difference between two profiles is $\Delta x=0.07H$. The experimental profiles for position $x=-0.774H$ are not available, and the LES profiles are presented here only to show the development of the predicted boundary layer at this position. The fine grid LES (denoted with a solid line) overlaps the experimental profiles at all positions except perhaps at the positions on the roof of the body (i.e., $x=-0.844H$ and $-0.705H$). The discrepancies on the roof probably stem from different Reynolds numbers in the experiments and our simulations. Although the flow separates on the leading edge of the front end of the body in our simulation, the separation region is very thin in both the streamwise and wall normal directions. There are no experimental observations of the flow around the front part of the body at the high Reynolds number, but it is reasonable to expect that the separation region becomes thinner as the Reynolds number is increased. Thus the flow on the roof is principally that of a turbulent boundary layer and is therefore defined by the viscosity. The Reynolds number in our LES is about four times lower than in the experiments, resulting in differences in boundary layer thicknesses. The influence of the Reynolds number is already reduced at the position directly after the upstream sharp edge of the slanted surface [i.e., the fourth profile from the left ($x=-0.635H$) in Fig. 7(*a*)] and the geometry starts to dictate the downstream flow. The coarse grid simulation (dashed-dotted curve in the figure) predicts very unrealistic flow far above the boundary layer with oscillations [see the third profile from the left in Fig. 7(*a*)]. It is interesting to observe how the change from attached to separated flow downstream of the fourth profile position ($x=-0.635H$) smooths these oscillations. Differences between profiles from our LES on the coarse and the medium grids and the experimental data are smaller in the region of the separation bubble than in the region after the reattachment on the slanted surface [see Fig. 7(*a*)]. The coarse grid simulation predicts too high a momentum above the slanted surface in the region after the reattachment (the first to the sixth profile from the right).

The $\langle W\rangle_t$ velocities along the slanted surface are in very good agreement with the experimental profiles for all three LES [see Fig. 7(*c*)]. Also here are some differences between simulations but they appear to be smaller than for the $\langle U\rangle_t$ velocities.

Figures 7(*b*) and 7(*d*) present $\langle U\rangle_t$ and $\langle W\rangle_t$ velocity profiles in the wake region behind the body for positions x equal to $0.059H$, $0.128H$, $0.132H$, $0.302H$, $0.306H$, $0.479H$, $0.653H$, $0.826H$, H, $1.174H$, $1.521H$, $1.868H$, and $2.215H$ from left to right. Let us first consider all profiles at all positions except $x=0.059H$, $0.128H$, and $0.302H$. Although the LES using the fine grid gives an almost exact representation of the experimental profiles, all three LES have predicted velocity profiles in very good agreement with the experimental data. Coarse LES have some difficulty giving an accurate representation of the lower recirculating region [see profiles at $x=0.132H$ and $x=0.306H$ in Fig. 7(*b*)] (i.e., the third and fifth profiles from the left, respectively) but the medium simulation manages to capture these regions very well. Let us now return to the remaining three positions (the first, second, and fourth profiles from the left, i.e., $x=0.059H$, $0.128H$, and $0.302H$). The experimental data for these profiles are denoted here with

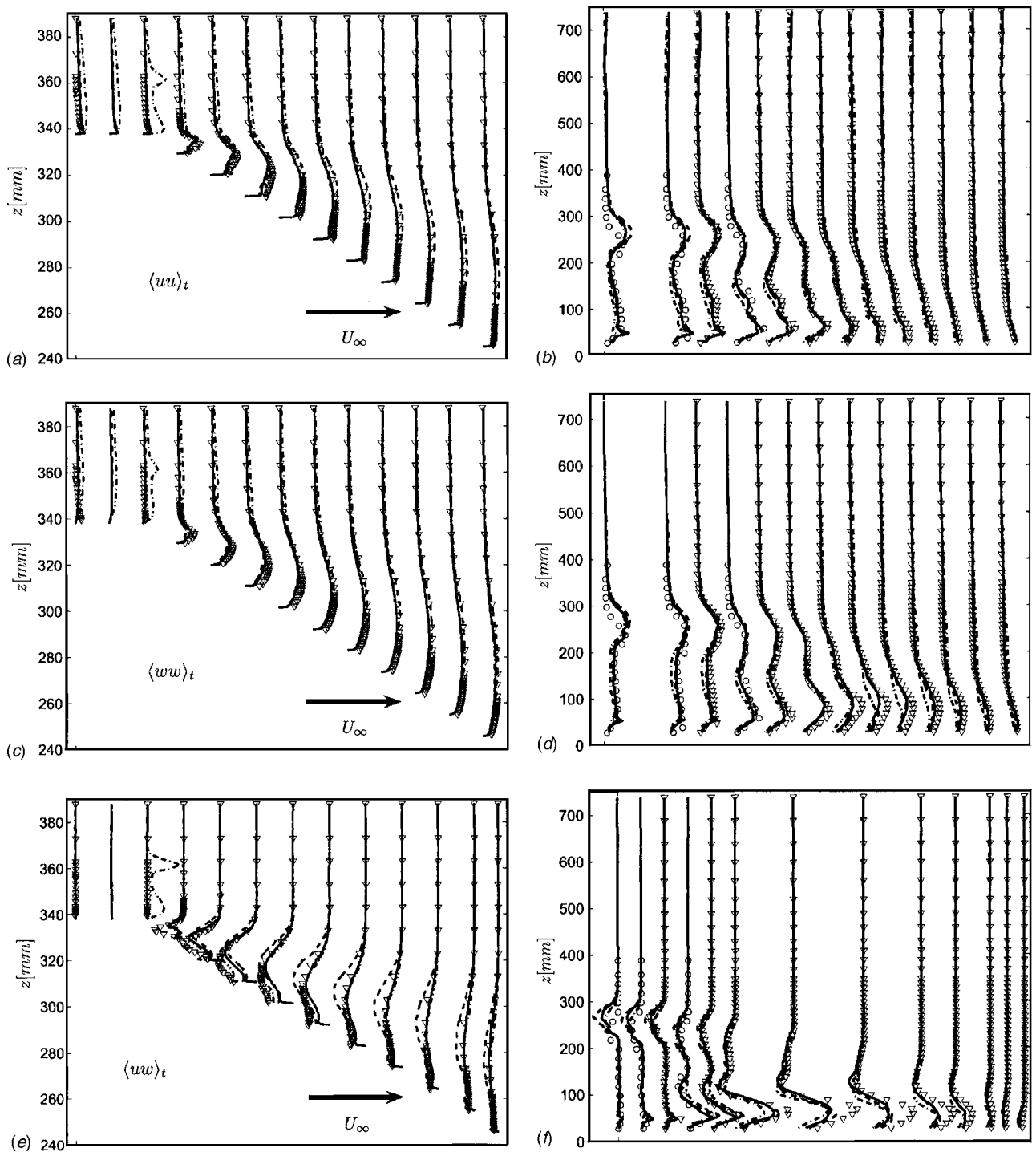

Fig. 8 Time-averaged Reynolds stresses in the symmetry plane ($y=0$). $\langle uu \rangle_t$ [(*a*) and (*b*)]; $\langle ww \rangle_t$ [(*c*) and (*d*)]; $\langle uw \rangle_t$ [(*e*) and (*f*)]. Left: slanted surface; right: wake region. Fine grid (solid curve); medium grid (dashed curve); coarse grid (dashed-dotted curve); experiment (symbols).

circles and come from a different data set than the one that contains all the other profiles in the wake. The experimental profiles for these positions are provided only up to $z=388$ mm compared to other profiles that go up to $z=738$ mm. All LES simulations are in relatively poor agreement with experiment in the upper part (between $z=200$ mm and $z=388$ mm) of the velocity profiles at these positions [see Figs. 7(*b*) and 7(*d*)]. Profiles $x=0.128H$ (the second profile from the left) and $x=0.302H$ (the fourth profile from the left) are located at positions only 1 mm from profiles in the first data set, $x=0.132H$ (the third profile) and $x=0.306H$ (the fifth profile), respectively. Yet the flow in the experimental data changes to a relative great extent between these almost identical positions. Furthermore, our LES using a fine grid gives exact representations of the experimental profiles from the first data set. We thus believe that something is wrong with the experimental data in the second data set (i.e., at positions $x=0.059H$, $0.128H$, and $0.302H$ in plane $y=0$).

Figure 8 presents a comparison between experimental and LES time-averaged Reynolds stresses $\langle uu \rangle_t$, $\langle ww \rangle_t$, and $\langle uw \rangle_t$ in the

center plane, $y=0$. We concentrate first on the flow above the slanted surface in Figs. 8(*a*), 8(*c*), and 8(*e*). The oscillations in the coarse LES of the flow above the roof (the first, second, and third profiles from the left) found in the velocity field are amplified here [see the third profile from the left in Figs. 8(*a*), 8(*c*), and 8(*e*)]. In addition, the normal Reynolds stresses are overpredicted in the flow above the roof in this coarse grid simulation [see $\langle uu\rangle_t$ and $\langle ww\rangle_t$ in the first three profiles from the left in Figs. 8(*a*) and 8(*c*)]. As we move downstream and pass the separation edge (profiles number four, five, etc.), the oscillations in the coarse LES disappear. All three LES produce slightly lower normal Reynolds stresses in the region of recirculating flow [see Figs. 8(*a*) and 8(*c*)], indicating that the experimental flow is slightly more unsteady than the simulated one. The part of the predicted profiles in the coarse grid LES that is located above the recirculating region displays slightly higher normal stresses [see the fourth, fifth, and sixth profiles from the left in Fig. 8(*a*) for $z>340$ mm], similar to what is seen in the upstream flow above the roof. The magnitude of the shear stress profiles $\langle uw\rangle_t$ in the separating region [see Fig. 8(*e*)] is somewhat underpredicted in our LES, but our LES still give much better prediction of these profiles than any of the simulations described in [5]. Profiles $\langle uw\rangle_t$ downstream of the reattachment on the slanted surface are very well captured with both the coarse and fine grid LES. Surprisingly, the medium grid simulation appears to give the worst prediction of the stresses at these positions.

The stresses in the wake flow in our LES are in good agreement with the experimental profiles [see Figs. 8(*b*), 8(*d*), and 8(*f*)]. Some differences between the fine grid LES and the experimental normal stresses are again visible for positions $x=0.059H$, $0.128H$, and $0.302H$ (the first, second, and fourth profiles coming from the different data set as compared to the other profiles). The coarse grid LES predicts a lower magnitude of the normal stresses in the lower part of the profiles at almost all positions (this is particularly visible in the region around the end of the near-wake separation bubble, i.e., the third to the seventh $\langle ww\rangle_t$ profiles from the right). The shear stresses $\langle uw\rangle_t$ are underpredicted in the region close to the rear point of the wake bubble [see Fig. 8(*f*)]. Some small differences between the LES and experimental $\langle uu\rangle_t$ and $\langle ww\rangle_t$ profiles are also visible at these positions [see Figs. 8(*b*) and 8(*d*)].

Let us now consider the results for two other planes, $y=0.35H$ and $y=0.63H$. Figures 9(*a*), 9(*c*), and 9(*e*) show comparisons of the velocity profiles above the slanted surface in plane $y=0.35H$. Unfortunately, measurements are not available close to the wall. Profiles in these figures are for the same x positions as in the center plane.

As in the profiles in the center plane, we find the unphysical oscillations in the flow above the boundary layer on the roof in the LES using the coarse grid [see Fig. 9(*a*)]. These oscillations are not damped directly after the separation on the sharp edge between the roof and the slanted surface as they are in the center plane [see profiles at the fourth to the eighth positions from the left in Fig. 9(*a*)]. Although we lack experimental data in the boundary layer, we find that the lower part of the streamwise velocities from our LES has a lower magnitude after the separation than the experimental profiles (if we extrapolate these down to the wall of the body).

The spanwise velocity components above the slanted surface are shown in Fig. 9(*c*). The magnitudes of these velocities are lower than the magnitudes of the streamwise components, and the LES profiles give an accurate representation of the experimental profiles (again it is not possible to judge the capability of our LES to predict the near-wall region due to the lack of the experimental data in this region).

The $\langle W\rangle_t$ velocities on the slanted surface in our LES are compared with the experimental data in Fig. 9(*e*). They are in very good agreement except very close to the separation edge [see $x=-0.635H$ and $x=-0.566H$ (i.e., the fourth and fifth profiles)].

Compared to the large number of x positions available in the center plane, only three profiles ($x=0.059H$, $0.128H$, and $0.302H$) are provided in plane $y=0.35H$ in the experiments of Lienhart and Becker [3]. Our LES give an accurate representation of all three velocity components [see Figs. 9(*b*), 9(*d*), and 9(*e*)]. The magnitudes of the $\langle U\rangle_t$ and $\langle W\rangle_t$ LES velocities are slightly lower in the medium part of the profiles at position $x=0.302H$ (the third profiles from the left), indicating a smaller recirculation of the near wake bubble. We have also found that the turbulent kinetic energy at this position is slightly lower in the LES compared to that measured in the experiment (not shown here) that indicates a more steady flow. The lower parts of the $\langle V\rangle_t$ profiles for positions $x=0.059H$ and $x=0.128H$ (i.e., the first and second profiles from the left) are better predicted using the fine and the medium grids than the coarse grid [see Fig. 9(*d*)]. Surprisingly, the $\langle W\rangle_t$ velocity at position $x=0.059H$ [the first profile from the left in Fig. 9(*f*)] in the case of the coarse grid has the best agreement with the experimental data. Again, this "better" agreement of one or two profiles from the coarser grid with the experimental data is only coincidental.

Comparisons of the velocity profiles in plane $y=0.63H$ are shown in Fig. 10. Both the $\langle U\rangle_t$ and the $\langle V\rangle_t$ velocities from the fine grid LES are in very good agreement with the experimental data at all positions in the flow above the slanted surface [see Figs. 10(*a*) and 10(*c*)]. Some differences are visible between the LES and the experimental $\langle W\rangle_t$ velocities at the positions between $x=-0.434H$ and $x=-0.08H$ [the seventh to eleventh profiles from the left in Fig. 10(*e*)]. The lower magnitude of the LES profiles at these positions indicates thinner, cone-like vortices that form at the rear slanted edges. The coarse grid simulation suffers from the poor resolution in the lower part of the slanted surface. This is particularly visible in the $\langle W\rangle_t$ profiles, where the profiles from the coarse grid LES are not able to follow the curved experimental profiles.

Figures 10(*b*), 10(*d*), and 10(*f*) present comparisons of the velocity profiles in the near wake at positions $x=0.059H$, $x=0.128H$, and $x=0.302H$, for which experimental data are available. The chief differences between our LES and the experimental profiles were found in the streamwise velocities, $\langle U\rangle_t$, for $z<50$ mm (thus in the wake flow below the body). The differences between these profiles can be explained by the differences in the geometries of the bodies used in the experiment and our numerical studies. The model used in the experiments was placed on four stilts with a diameter of 30 mm at positions $y=\pm 163.5$ mm. Thus the extension of the stilts was up to $y=\pm 178.5$ mm, which is very close to the position ($y=180$ mm) of the profiles in Fig. 10. Although the rear pair of stilts is located relatively far from the near wake (at $x=-1.292H$), the resulting wake behind the stilts decreases the streamwise velocity in the experiment.

Another influence of the stilts is the unsteadiness of their wakes. The profiles of the turbulent kinetic energy (Fig. 11) show that, while the flow in our LES is almost steady ($\langle k\rangle_t \sim 0$) below the body, the flow measured in the experiments has relatively high turbulent kinetic energy in this region (particularly for the first profile from the left, i.e., $x=0.059H$). The turbulent kinetic energy in the experimental flow may be the consequence of the unsteadiness in the wake behind the stilts.

9 Conclusions

The large eddy simulation technique has yet not matured sufficiently to be used to obtain design quantities in the external aerodynamics of the ground vehicles, such as drag or lift. Its use is prohibited by the requirement on resolution in the near-wall region. Several promising approaches that reduce resolution requirements by their modeling of the near-wall region are under devel-

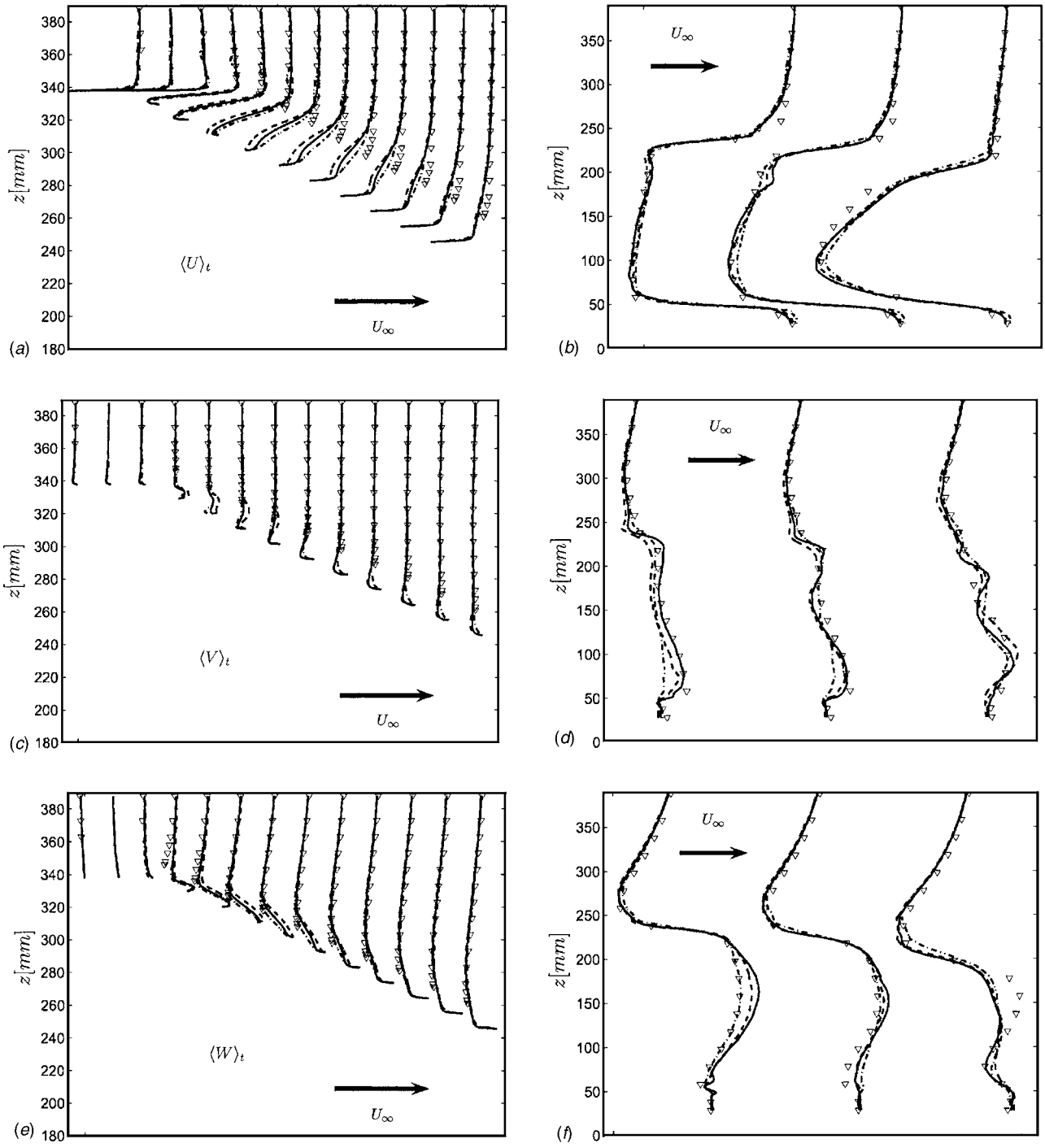

Fig. 9 Time-averaged $\langle U\rangle_t$ [(*a*) and (*b*)], $\langle V\rangle_t$ [(*c*) and (*d*)], and $\langle W\rangle_t$ [(*e*) and (*f*)] velocity profiles in plane $y=0.35H$. Left: slanted surface; right: wake region. Fine grid (solid curve); medium grid (dashed curve); coarse grid (dashed-dotted curve); experiment (symbols).

opment. Among these are the hybrid methods, so-called hybrid LES-RANS or detached eddy simulations (DES), that use RANS solution in the near-wall region and the LES in the rest of the domain. Unfortunately these are still not fully developed and several problems remain to be solved (such as choice of turbulence model, where to put the matching line between the RANS and the LES regions, how to provide the correct boundary conditions for the LES region from the RANS region, etc.) before they can be used in vehicle aerodynamics.

Some alternative approaches in using LES in vehicle aerodynamics are thus needed. This paper has suggested one approach that uses the constraints that are put on the flow by the geometry, such as separation defined by the sharp edge. It has been assumed that the Reynolds number and the resolution requirements could be decreased if the positions of the recirculating regions in the flow are defined by the geometry rather than by the viscosity and the upstream conditions (such as turbulence at the inlet and the boundary layer thickness).

Our approach was tested on the flow around a generic car (a so-called Ahmed body) with the angle of the rear slanted surface of 25%. Earlier RANS and LES applications in this flow have been unsuccessful [5]. The Reynolds number was decreased about

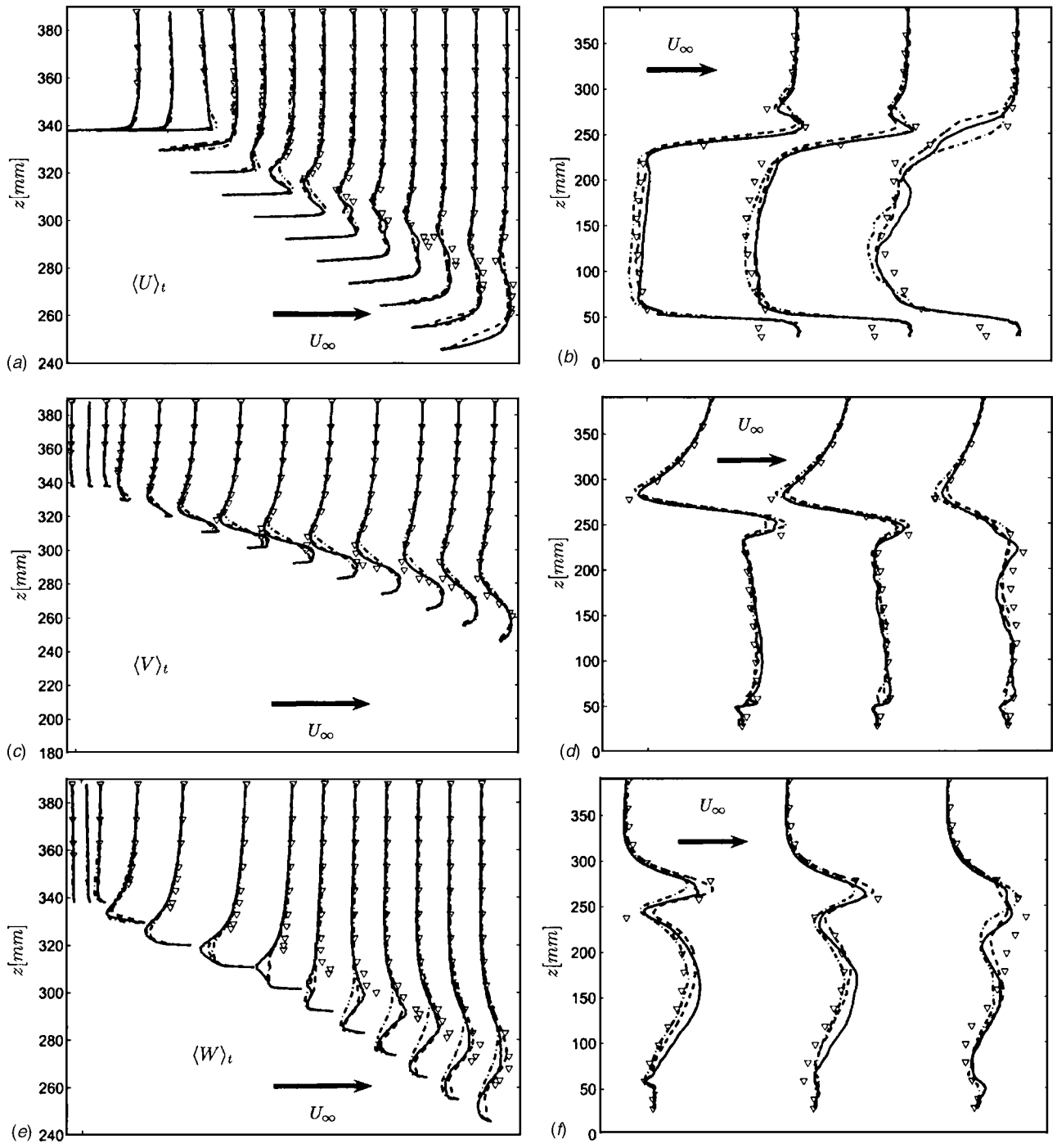

Fig. 10 Time-averaged $\langle U \rangle_t$ [(*a*) and (*b*)], $\langle V \rangle_t$ [(*c*) and (*d*)], and $\langle W \rangle_t$ [(*e*) and (*f*)] velocity profiles in plane $y=0.63H$. Left: slanted surface; right: wake region. Fine grid (solid curve); medium grid (dashed curve); coarse grid (dashed-dotted curve); experiment (symbols).

four times in our LES as compared with the experimental one [3]. Although the experimental setup included a turbulent trip wire that was glued to the front end of the model, making the flow relatively Reynolds number independent, there are still differences in the experimental and simulated boundary layers on the body. However, our results show that the dependence on the results in the wake, after the separations at the sharp edges, of the Reynolds number is very small.

An extensive comparison has been given of our LES results and the experimental data. This comparison confirmed our assumptions and the usefulness of the new LES approach that we suggest. Only small discrepancies were found between our LES and experimental results, and some of these are believed to be problems in the experiments.

This paper showed that the flow around an Ahmed body (and especially the flow after its sharp edge separations) at high Reynolds number can be simulated using LES at lower Reynolds number. We believe that the main reason for this relative Reynolds number independence of the flow around and behind the rear of the body are the sharp edge separations in combination with the tripping of the turbulent boundary layer at the front of the body in the experiments. We must stress that there is nothing in this paper

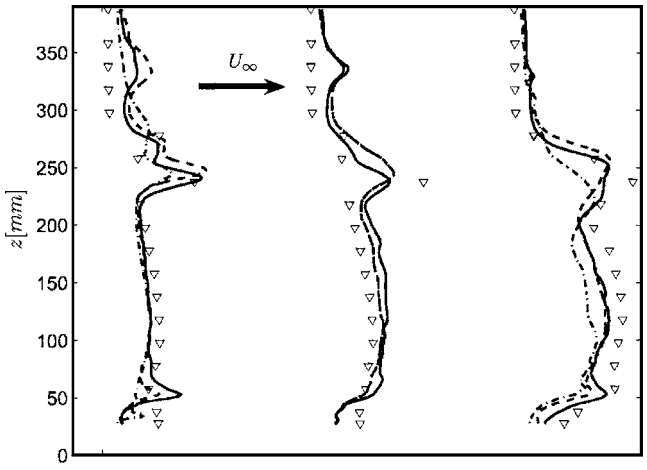

Fig. 11 Time-averaged turbulent kinetic energy $\langle \bar{k} \rangle_t$ in plane $y=0.63H$. Fine grid (solid curve); medium grid (dashed curve); coarse grid (dashed-dotted curve); experiment (symbols).

that shows that this method is general and will work for flow around vehicles with smooth surface separations. The present paper shows only that the method is useful in the such flows as are studied in this paper, i.e., the flow around bodies where the separations are defined by the geometry.

Now that we have proved the accuracy of our LES in adequately representing the flow around the generic car body, we shall in [14] use the LES results to explore this flow in detail.

Acknowledgments

This work was supported by the FLOMANIA project. The FLOMANIA (Flow Physics Modeling—An Integrated Approach) is a collaboration between Alenia, AEA, Bombardier, Dassault, EADS-CASA, EADS-Military Aircraft, EDF, NUMECA, DLR, FOI, IMFT, ONERA, Chalmers University, Imperial College, TU Berlin, UMIST, and St. Petersburg State University. The project is funded by the European Union and administrated by the CEC, Research Directorate-General, Growth Programme, under Contract No. G4RD-CT2001-00613. Computer time on the Linux cluster, provided by the NSC (National Supercomputer Center in Sweden), is gratefully acknowledged.

References

[1] Ahmed, S. R., Ramm, G., and Faltin, G., 1984, "Some Salient Features of the Time Averaged Ground Vehicle Wake," SAE paper no. 840300.
[2] Spohn, A., and Gillieron, P., 2002, "Flow Separations Generated by a Simplified Geometry of an Automotive Vehicle," in *IUTAM Symposium: Unsteady Separated Flows*, April 8–12, Toulouse, France.
[3] Lienhart, H., and Becker, S., 2003, "Flow and Turbulent Structure in the Wake of a Simplified Car Model," SAE paper no. 2003-01-0656.
[4] Han, T., 1989, "Computational Analysis of Three-Dimensional Turbulent Flow Around a Bluff Body in Ground Proximity," AIAA J., **27**(9), pp. 1213–1219.
[5] Manceau, R., and Bonnet, J.-P., 2000, 10th Joint ERCOFTAC (SIG-15)/IAHR/QNET-CFD Workshop on Refined Turbulence Modelling, Poitiers.
[6] Krajnović, S., and Davidson, L., 2003, "Numerical Study of the Flow Around the Bus-Shaped Body," ASME J. Fluids Eng., **125**, pp. 500–509.
[7] Krajnović, S., 2002, "Large Eddy Simulations for Computing the Flow Around Vehicles," Ph.D. thesis, Chalmers University of Technology, Gothenburg.
[8] Cooper, K. R., 1985, "The Effect of Front-Edge Rounding and Rear Edge Shaping on the Aerodynamic Drag of Bluff Vehicles in Ground Proximity," SAE paper no. 850288.
[9] Smagorinsky, J., 1963, "General Circulation Experiments with the Primitive Equations," Mon. Weather Rev., **91**(3), pp. 99–165.
[10] Krajnović, S., and Davidson, L., 2002, "Large Eddy Simulation of the Flow Around a Bluff Body," AIAA J., **40**(5), pp. 927–936.
[11] Davidson, L., and Farhanieh, B., 1995, "CALC-BFC: A Finite-Volume Code Employing Collocated Variable Arrangement and Cartesian Velocity Components for Computation of Fluid Flow and Heat Transfer in Complex Three-Dimensional Geometries," Report 95/11, Department of Thermo and Fluid Dynamics, Chalmers University of Technology, Gothenburg.
[12] Rhie, C. M., and Chow, W. L., 1983, "Numerical Study of the Turbulent Flow Past an Airfoil with Trailing Edge Separation," AIAA J., **21**(11), pp. 1525–1532.
[13] Nilsson, H., and Davidson, L., 1998, "CALC-PVM: A Parallel SIMPLEC Multiblock Solver for Turbulent Flow in Complex Domains," Internal report 98/12, Department of Thermo and Fluid Dynamics, Chalmers University of Technology, Gothenburg.
[14] Krajnović, S., and Davidson, L., 2005, "Flow Around a Simplified Car, Part 2: Understanding the Flow," ASME J. Fluids Eng., **127**, pp. 919–928.
[15] Sims-Williams, D. B., and Dominy, R. G., 1998, "Experimental Investigation into Unsteadiness and Instability in Passanger Car Aerodynamics," SAE paper no. 980391.
[16] Lienhart, H., 2004, private communication, Universität Erlangen-Nürnberg.